Physica Medica 73 (2020) 29–42

Contents lists available at ScienceDirect

Physica Medica

journal homepage: www.elsevier.com/locate/ejmp

Original paper

A microdosimetric analysis of the interactions of mono-energetic neutrons with human tissue

C.M. Lund[a,*], G. Famulari[a], L. Montgomery[a], J. Kildea[a]

[a] Medical Physics Unit, McGill University, Montreal, QC H4A3J1, Canada

ARTICLE INFO

Keywords:
Neutrons
Microdosimetry
Monte Carlo
Track structure

ABSTRACT

Nuclear reactions induced during high-energy radiotherapy produce secondary neutrons that, due to their carcinogenic potential, constitute an important risk for the development of iatrogenic cancer. Experimental and epidemiological findings indicate a marked energy dependence of neutron relative biological effectiveness (RBE) for carcinogenesis, but little is reported on its physical basis. While the exact mechanism of radiation carcinogenesis is yet to be fully elucidated, numerical microdosimetry can be used to predict the biological consequences of a given irradiation based on its microscopic pattern of energy depositions. Building on recent studies, this work investigated the physics underlying neutron RBE by using the microdosimetric quantity dose-mean lineal energy ($\bar{y}_D$) as a proxy. A simulation pipeline was constructed to explicitly calculate the $\bar{y}_D$ of radiation fields that consisted of (i) the open source Monte Carlo toolkit Geant4, (ii) its radiobiological extension Geant4-DNA, and (iii) a weighted track-sampling algorithm. This approach was used to study mono-energetic neutrons with initial kinetic energies between 1 eV and 10 MeV at multiple depths in a tissue-equivalent phantom. Spherical sampling volumes with diameters between 2 nm and 1 μm were considered. To obtain a measure of RBE, the neutron $\bar{y}_D$ values were divided by those of 250 keV X-rays that were calculated in the same way. Qualitative agreement was found with published radiation protection factors and simulation data, allowing for the dependencies of neutron RBE on depth and energy to be discussed in the context of the neutron interaction cross sections and secondary particle distributions in human tissue.

1. Introduction

1.1. Neutrons in radiotherapy

Radiation carcinogenesis is a major concern in radiological protection. In radiobiological terms, it is said to be a stochastic effect, meaning that the severity of the incurred cancer is independent of dose; only the likelihood of occurrence is dose-dependent. Furthermore, the so-called linear-no-threshold (LNT) principle states that even a small amount of ionizing radiation may induce sufficient mutations and genetic instability to initiate the process of carcinogenesis [1]. Thus, it is important to limit exposure to ionizing radiation to only those cases where it is justified, in that the anticipated benefits outweigh the biological risk. In external beam radiotherapy treatments, for example, the curative potential of ionizing radiation provides a significant medical benefit for cancer patients. However, the radiation cannot be contained to just the tumour volume and will necessarily deposit dose within normal tissues. This dose arises from in-field radiation as the planned treatment beam propagates through the patient as well as from out-of-field radiation due to leakage and scattering. A proper assessment of the long-term risk of stochastic effects is thus an important factor when considering the overall benefit of a proposed radiotherapy treatment [2]. During high-energy radiotherapy with photons (HERTX, $\gtrsim$ 8 MeV), the out-of-field component contains neutrons as a result of photo- and electro-nuclear reactions within the treatment equipment, the patient, and throughout the room [3,4]. Consequently, the patient is subjected to a whole-body, non-curative dose of neutrons that poses a risk for iatrogenic carcinogenesis [5].

In order to assess the carcinogenic risk posed by out-of-field neutrons, their relative biological effectiveness (RBE) for stochastic effects must be taken into account. However, the complexity of the progression from radiation insult to cancerous lesion makes radiation carcinogenesis difficult to predict quantitatively. Indeed, much of our understanding of carcinogenic risk comes not from a fundamental description, but from epidemiological investigations and extrapolations from experiments with animals. Many of these studies are encapsulated in the radiation weighting factors published by the International Commission on Radiological Protection (ICRP) [1] and the *Q* factors

* Corresponding author.
E-mail address: christopher.lund@mail.mcgill.ca (C.M. Lund).

https://doi.org/10.1016/j.ejmp.2020.04.001
Received 30 October 2019; Received in revised form 5 March 2020; Accepted 2 April 2020
Available online 10 April 2020

published by the United States Nuclear Regulatory Commission (US NRC) [6]. These factors are necessarily non-specific in that they were informed by results obtained with a wide variety of doses, dose rates, geometries, and other factors known to affect RBE. Although not in quantitative agreement, both sets of factors predict a marked energy dependence of neutron RBE. However, relatively little has been reported on the physical basis for this dependence or how it may vary with geometry and depth. At the root of this problem is that radiobiological experiments typically do not provide sufficient information to examine the impact of the various interactions between neutrons and tissue. Instead, a more fundamental approach must be taken.

1.2. Microdosimetry as a radiobiological tool

Recent advancements in computational power allow for fundamental studies of the relationship between radiation interactions and induced DNA damage [7]. Starting from a detailed description of radiation transport through biological tissue, techniques such as microdosimetry, clustering algorithms [8], and, more recently, multi-scale DNA damage simulations [9–13] have been developed in order to correlate physical interaction data with observed biological effects. In this work, a microdosimetric approach was taken. The application of microdosimetry to radiobiology, radiation protection, and radiation therapy is well established. For example, microdosimetric observables have been successfully used to predict the clinical effectiveness of neutron beams [14–16], proton beams [17], and carbon ion beams [18]. Additionally, they have been linked to biological endpoints such as chromosome damage in human cells [19] and cell survival in early responding tissues [20,21], and have been used to show agreement between Japanese A-bomb data and the carcinogenic risk of occupationally exposed miners [22]. Indeed, microdosimetry has even been recommended for investigating situations in which the biological effectiveness is not well characterized [23].

Much of the motivation for the use of microdosimetry as a radiobiological tool rests on the theory of dual radiation action (TDRA) [24,25], which provides a mathematical link between microdosimetric distributions and dose–effect relations such as RBE for cell survival. More specifically, the TDRA characterises the correlation between track structure and biological effect by considering the interplay of sub-lesions which, on their own, do not cause lasting damage. Variations in microdosimetric parameters can then be seen as adjustments in the range over which individual sub-lesions are able to interact and together cause the biological effect. Furthermore, the sub-lesion interactions can be subdivided into those that occur between sub-lesions resulting from the same track (intra-track, single event) and those arising from different tracks (inter-track, multi-event). In the case of low dose and low dose-rate environments, the assumption can be made that sensitive sites (e.g. cell nuclei) will only be crossed by single particle tracks and thus inter-track effects can be ignored. Under such conditions, the TDRA predicts that single-event microdosimetric distributions can be used to approximate RBE. Wuu et al. [26] utilised this formalism in their prediction of the RBE of low dose-rate brachytherapy sources, stating that:

$$\mathrm{RBE}_{\mathrm{isotope}} = \frac{\bar{y}_{D,\mathrm{isotope}}}{\bar{y}_{D,\mathrm{ref}}} \tag{1}$$

where $\bar{y}_D$ is the single-event microdosimetric quantity dose-mean lineal energy, ‘isotope’ refers to the radioactive source under study, and ‘ref’ refers to the chosen reference radiation.

1.3. Predicting neutron RBE

For neutrons, the ‘low dose’ assumption actually holds to very high neutron doses [24] and is even used in clinical situations wherein the RBE for late toxicities is assessed by lineal energy for fast neutron therapy beams [27]. The assumption can thus be made that the neutron environment experienced by patients undergoing HERTX meets the ‘low dose environment’ criteria and the biological consequences of such neutron exposures therefore arise from the single event action of radiation. Consequently, the energy dependence of the carcinogenic risk posed by out-of-field neutrons can be investigated by comparing the $\bar{y}_D$ of mono-energetic neutrons to that of a reference radiation.

This approach was recently taken by Baiocco et al. [28] as part of the ANDANTE project’s [29] effort to discern an *ab initio* model of neutron RBE. Utilising the microdosimetric function of the PHITS [30] Monte Carlo (MC) toolkit, they calculated microdosimetric parameters for a large range of neutron energies as the neutrons interacted within a standardised human tissue phantom (see Section 2.4) [28]. By comparing their results with published neutron weighting factors, Baiocco et al. [28] were able to identify and examine the interplay of some key neutron interactions responsible for the large variation in neutron RBE with energy. We aim to build on their microdosimetric work by focusing and expanding the analysis within an energy range relevant to HERTX (1 eV-10 MeV). To do so, we have constructed a Geant4 [31–33]-based simulation pipeline consisting of both condensed-history MC and track-structure MC (MCTS) phases. The extensible nature of Geant4 allowed us to implement a recently published microdosimetric analysis algorithm [34] while also providing access to much of the most recent progress in MCTS cross sections and physics models.

2. Materials and methods

This section provides a brief overview of the microdosimetric theory (Section 2.1) and and numerical techniques (Section 2.2) relevant to this work before describing the details of the developed simulation pipeline.

2.1. Microdosimetric quantities

Microdosimetric quantities are determined by considering the intersection of particle track structures with sampling volumes representative of biological targets. For a given intersection, or event, the lineal energy y is calculated by dividing the single-event imparted energy ϵ_s by the mean chord length $\bar{\ell}$ of the sampling volume [35]:

$$y = \frac{\epsilon_s}{\bar{\ell}} \tag{2}$$

The expectation value of lineal energy is calculated as:

$$\bar{y}_F = \int_0^\infty y f(y) dy \tag{3}$$

where $f(y)$ is the relative frequency distribution, i.e. the probability density function describing the probability that a measurement will yield a lineal energy value between y and $y + dy$. The dose-mean lineal energy is the first moment of $d(y) = y f(y)/\bar{y}_F$:

$$\bar{y}_D = \int_0^\infty y d(y) dy \tag{4}$$

$d(y)$ is typically referred to as the dose distribution because it represents the probability that ϵ_s is deposited (as dose) by lineal energy values between y and $y + dy$ [36]. From the definition of $d(y)$, Eq. 4 can be rewritten as:

$$\bar{y}_D = \frac{1}{\bar{y}_F} \int_0^\infty y^2 f(y) dy \tag{5}$$

Thus, $\bar{y}_D$ can be calculated through knowledge of the relative frequency distribution by taking the ratio of its second moment to its first [37].

Although $\bar{y}_D$ is defined for both uncharged and charged particles, it only accounts for energy transfers from charged particle interactions. In order to calculate the $\bar{y}_D$ of an uncharged particle field, the effects of its various secondaries must be determined and combined [38]. To do so,

one must weight the $\bar{y}_D$ of each secondary species by its relative dose contribution (fraction of total dose). Furthermore, the $\bar{y}_D$ of a given particle varies with energy, so one must ensure that the energy dependence of the species' own dose distribution is taken into account when calculating the overall $\bar{y}_D$ of the species' polyenergetic spectrum. In this work, the latter was accomplished by way of the local approximation (wherein absorbed dose is assumed equal to electronic kerma). Under conditions where the local approximation holds, the initial spectrum of a secondary species is representative of the energy-dependence of its dose distribution. Therefore, calculating the $\bar{y}_D$ of a population of tracks generated by randomly sampling their initial kinetic energies from the initial spectrum provides the $\bar{y}_D$ of this spectrum directly. This allows for the $\bar{y}_D$ of the uncharged field to be obtained from its collection of secondary species i by:

$$\bar{y}_D = \sum_i d_i \bar{y}_{D,i} \tag{6}$$

where d_i is the relative dose contribution of the species. Thus, neutron $\bar{y}_D$ can be obtained without requiring an explicit calculation of the energy distributions of each d_i or $\bar{y}_{D,i}$, as these are accounted for implicitly.

2.2. Weighted track sampling

In numerical microdosimetry, the complete population of generated charged particle tracks is available for study with any number of sampling volumes. An efficient method of obtaining statistically-relevant microdosimetric observables is to repeatedly sample each track and to bias this sampling by only placing volumes within the associated volumes of the tracks [39]. This is in contrast to randomly overlaying sampling volumes across the entire volume under study according to a uniform spatial distribution.

The associated volume of a track is defined as the region around it in which the sampling efficiency is 1 [40]. That is to say, any sampling volume centred within the associated volume is guaranteed to contain at least one relevant transfer point (interaction site at which energy was transferred), while any volume centred outside of the associated volume will not contain any [41]. In the case of spherical sampling, the associated volume is constructed by centring a sphere of the chosen sampling radius (the associated sphere or region) at each transfer point and taking their union [26].

Weighted sampling techniques can be used to ensure points fall within the associated volume without introducing statistical biases [37]. To sample the tracks, one first selects a transfer point at random and then selects a position within the associated region at which to centre a sampling volume [41]. For spherical sampling volumes, one defines a radial offset d less than the sampling radius r and applies it along a random direction to choose the centre position. One may then calculate ϵ_s by summing over all energy deposits that occurred within a distance r of the chosen position and subsequently determine the y for the event. This process is depicted in Fig. 1. However, this technique is biased towards areas that are densely populated with transfer points. To correct for this bias, the calculated ϵ_s for a given sampling volume must be weighted by the inverse of the number of transfer points that fell within that volume [40].

An advantage of considering single event quantities such as y is that tracks can be processed individually. Thus, both track generation and analysis were multi-threaded in this work, which significantly reduced the amount of data to be stored or accessed at a given time. However, treating tracks independently exacerbates a subtle issue with weighted sampling. Unless the entire population of tracks is considered when choosing a transfer point about which to place a sampling volume, the relative size of the tracks cannot be taken into account. When sampling uniformly across all tracks simultaneously, larger tracks are more likely to be intersected by sampling volumes than smaller tracks. Famulari et al. [34] thus introduced an associated volume weight; an approach that requires a method for calculating the associated volume of arbitrarily sized and shaped tracks. An approximate calculation based on a discretisation of the sampling spheres into sub-voxels has been implemented and its details are given in Section 2.5.

2.3. Pipeline overview

Due to the complexities of neutron moderation, it was necessary to employ a simulation geometry of representative size and composition. While MCTS simulations are necessary for accurate microdosimetry on the scale of sub-cellular structures [42] and thus for the study of DNA damage, available MCTS codes are computationally expensive and confined almost entirely to studies in water. To circumvent these limitations, condensed-history simulations were performed upstream to both narrow the scope of the MCTS simulations and to allow for the use of tissue-equivalent material (Section 2.4). From the condensed-history simulations, the initial spectra (kinetic energies at the point of liberation) of the secondary species and their relative dose contributions were obtained. These spectra were then used as the input energies for the generation of particle tracks via MCTS. To obtain the microdosimetric observables, a weighted track sampling algorithm described by Famulari et al. [34] was implemented directly into the MCTS simulation and used to calculate $\bar{y}_D$ (Section 2.5). An overview of this simulation pipeline is given in Fig. 2. To perform the simulations, the open source MC toolkit Geant4 and its radiobiological extension Geant4-DNA [43–46] were chosen largely due to their customizable nature. All simulations were performed with Geant4 v10.04.p02.

2.4. Condensed history simulations

Mono-energetic neutron sources with initial kinetic energies between 1 eV and 10 MeV were distributed uniformly across the surface of a 40 cm radius sphere (world) of low density gas used to approximate vacuum. At the centre of the world was an implementation of the four-component soft tissue-equivalent sphere recommended by the International Commission on Radiation Units and Measurements (ICRU) for use in radiation safety and dosimetry applications [47] (Fig. 2, left). Intended to approximate a human adult torso, this ICRU-4 sphere is 30 cm in diameter and comprised of hydrogen, carbon, nitrogen, and oxygen. Consistent with the work of Baiocco et al. [28], three spherical scoring volumes of radius 1.5 cm made of the same ICRU-4 material were centred along a single axis at radial distances of 0 cm, 7.5 cm, and 13.5 cm from the phantom's centre. Throughout the rest of this paper, these volumes will be referred to as the inner, intermediate, and outer scoring volumes, respectively. The emissions of the neutron sources were biased by a cosine-law angular distribution to correct against the inverse square law and impinged upon the ICRU-4 sphere.

The Lawrence Livermore evaluated data libraries for photons [48], electrons [49], and atomic relaxation [50] were used to handle electromagnetic processes. Default models were included to handle less dosimetrically significant reactions such as free neutron decay (`G4DecayPhysics`) and the decay of radioactive isotopes (`G4RadioactiveDecayPhysics`). The Geant4 `ParticleHP` models were used to describe hadronic elastic scattering and inelastic processes (scattering, neutron capture, fission). These models rely on tabulated data from the US Evaluated Nuclear Data Files (ENDF/B) [51] for both cross sections and final state determination [33]. Below 4 eV, an additional elastic scattering dataset (`G4ParticleHPThermalScattering`) was incorporated to improve the transport of thermal neutrons.

As neutrons interact with a medium, they produce fields of secondary gammas, protons, and heavier charged particles with complex energy spectra. Due to the short ranges and low radiative yields of the secondary charged particles, neutron dose is approximately equivalent to electronic kerma when charged particle equilibrium (CPE) exists

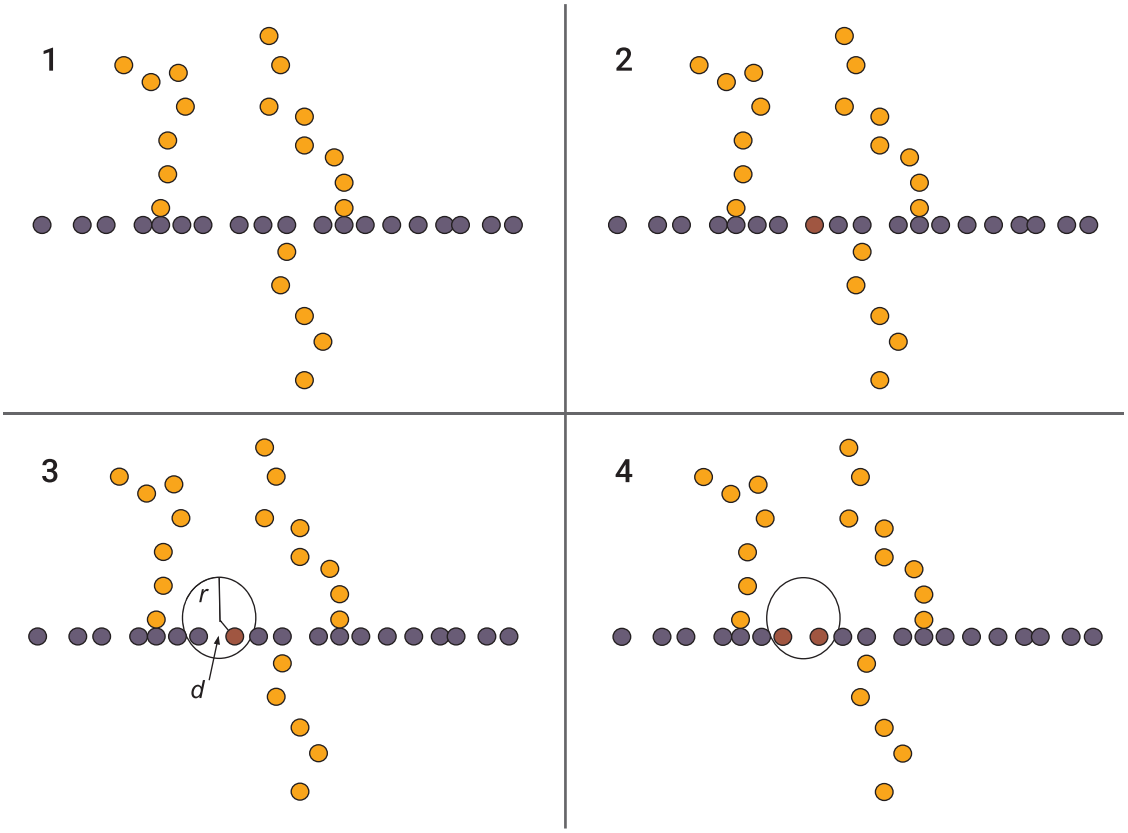

Fig. 1. The weighted sampling method consists of the following steps: (1) track generation (transfer points of primary ions in purple and of delta electrons in orange), (2) the random choice of a transfer point (highlighted in red), (3) the placement of a sampling volume at a distance $d < r$ from the point, and (4) the summation of all energy deposits within this volume. Weights are then applied to correct for statistical biases (track size and transfer point density) and the process is repeated.

[52]. This allows for the use of the so-called local approximation, which is believed to hold for neutron fields in the ICRU sphere up to about 20 MeV [53] because of the negligible attenuation of the neutrons over the maximum range of their charged secondaries (see Andreo et al. [54]). In MC, the local approximation is accomplished by killing particles at their point of generation and considering their kinetic energies to be deposited on the spot. Therefore, the relative dose contributions could be calculated from the kinetic energies of the charged particles at their points of liberation. This allowed for the simultaneous acquisition of spectra and relative dose data, while also greatly

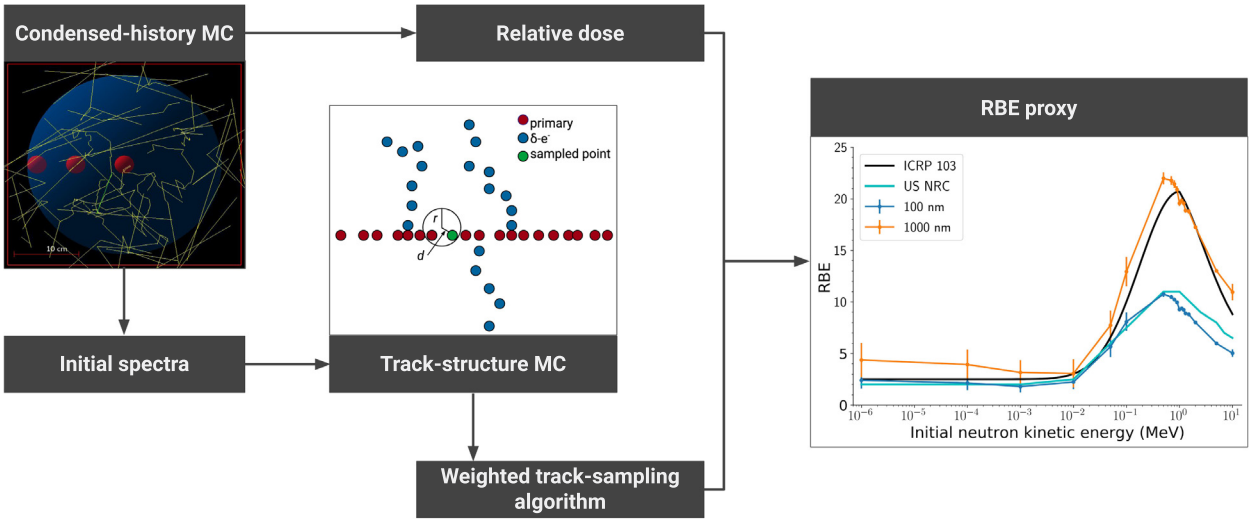

Fig. 2. A simplified schematic of the neutron microdosimetry simulation pipeline developed in this work. The initial spectra and relative dose contributions of the secondary species produced by mono-energetic neutrons were collected within three scoring volumes centred at different depths within a human tissue-equivalent phantom using condensed-history MC (Geant4). The spectra were then used to determine the initial energy distribution of particle tracks that would be generated using MCTS (Geant4-DNA). Tracks were analysed individually via the weighted track-sampling algorithm and the $\bar{y}_D$ value of each relevant spectra was obtained for multiple sampling sphere diameters. Combining the individual $\bar{y}_D$ values with their appropriate relative dose contributions yielded the overall neutron $\bar{y}_D$ for each volume as a function of energy and sampling sphere diameter. Comparing neutron $\bar{y}_D$ to that of a reference radiation yielded a prediction of neutron RBE in accordance with the theory of dual radiation action.

reducing the simulation time. When a charged particle was liberated within a scoring volume, its kinetic energy was added to an associated histogram as well as to a running sum of the species' dose contribution. The histograms contained 500 logarithmically-spaced bins between 1 eV and 10 MeV. Special consideration was given to high-energy ($\gtrsim$1 MeV) electrons because Geant4-DNA does not presently allow for the transport of electrons with kinetic energies greater than 1 MeV. Thus, these electrons could not be killed immediately after generation and were instead tracked down to 1 MeV with Geant4, at which point they were considered to deposit their energies locally. All higher-order electrons produced during this slowing down process were passed to the MCTS phase as independent tracks. Thus, high-energy electrons were treated as a collection of uncorrelated lower-energy electrons when their spectra and dose contributions were recorded.

This process was repeated for a reference radiation of mono-energetic 250 keV X-rays.

2.5. Track structure simulations

Source particles for the MCTS simulations were obtained by sampling from the secondary particle distributions generated during the condensed-history phase. For every (i) particle type, (ii) scoring volume, and (iii) initial neutron particle energy, the corresponding distribution was repeatedly sampled to generate a set of source particles for a simulation of 10,000 independent tracks. Within each simulation, the sampled particles were emitted isotropically from the centre of a 40 km radius (i.e. semi-infinite) sphere composed of liquid water.

A custom physics constructor was written for the handling of charged particle interactions in the MCTS code. Between 10 keV and 1 MeV, the default `G4EMDNAPhysics` models were employed for electron interactions, while below 10 keV models from `G4EmDNAPhysics_option4` were used. With this combination, excitation and ionization events for all electron energies were handled by an implementation of the Emfietzoglou model of the dielectric function of liquid water [55] featuring low-energy corrections of varying detail [56]. Elastic scattering was handled by the Champion partial wave interpolated model [57] above 10 keV and by a screened Rutherford analytical model supplemented by an experimentally-derived screening parameter from Uehara et al. [58] below 10 keV [43]. Models for vibrational excitation (2 eV – 100 eV) and electron attachment (4 eV – 13 eV) were also included that were based on data from Michaud et al. [59] and Melton [60], respectively. Electrons were tracked down to 10 eV at which point they were killed and their energies deposited locally. The Geant4-DNA models for the transport of ions heavier than electrons are common to all provided physics lists; no alterations were made in this work. These cover nuclear scattering, excitation, ionisation, and charge-exchange processes, allowing for the tracking of protons and alpha particles (among other ions) down to 100 eV. Atomic relaxation was handled by the same Livermore models as described in Section 2.4. All gammas were killed because it was assumed that their energies were radiated far enough away that their energy depositions were no longer correlated with their particle tracks.

Every interaction that involved a non-zero local energy deposit was identified during the generation of each primary track. At each of these relevant transfer points, the incident particle's kinetic energy, initial position, and final position were recorded, along with the total energy deposited. The correlated secondary tracks were scored in the same manner and thus the full track structure associated with each primary particle was obtained.

The weighted track sampling algorithm was implemented using sampling spheres with diameters of 2 nm, 10 nm, 30 nm, 100 nm, and 1000 nm. All tracks were sampled $M = 1000$ times for each sampling radius r. The transfer point density weight $w_{\mathrm{tp},ij}$ of each sampled transfer point i of track j was equal to the reciprocal of the number of transfer points in its corresponding sampling sphere. After the track had been sampled M times, the weights were applied to the corresponding imparted energies and squared imparted energies in order to calculate the weighted lineal energy and weighted square lineal energy of the track:

$$y_j = \frac{\sum_{i=1}^{M} \epsilon_{ij} w_{\mathrm{tp},ij}}{\overline{\ell}_j \sum_{i=1}^{M} w_{\mathrm{tp},ij}};\ y_j^2 = \frac{\sum_{i=1}^{M} \epsilon_{ij}^2 w_{\mathrm{tp},ij}}{\overline{\ell}_j{}^2 \sum_{i=1}^{M} w_{\mathrm{tp},ij}} \tag{7}$$

where $\overline{\ell} = 4r/3$ was the mean chord length of the sampling sphere that was used.

In order to calculate the $\overline{y}_D$ of the particle species, an associated volume weight $w_{\mathrm{av},j}$ was calculated for each track j. This calculation was done by first translating the transfer point positions into coordinates on a grid composed of voxels with side length $2r/3$. The list of voxel coordinates was then filtered to eliminate redundant entries. Each of the remaining voxels was set as the centre of a cube with 27 subdivisions by padding along x, y, and z (creating a mesh). Once all cubes had been formed, repeated coordinates were filtered out and the volume of the remaining subdivisions was calculated. In this way, a cube with side length $2r$ (i.e. the cube circumscribed by the sampling sphere) was centred on each position and the union of the set was calculated and used as the associated volume weight. The $\overline{y}_D$ of the particle species was calculated by first multiplying the associated volume (weight) of each track by its weighted lineal energy y_j and weighted square lineal energy y_j^2, then summing over all N tracks:

$$\overline{y}_D = \frac{\sum_{j=1}^{N} y_j^2 \frac{w_{\mathrm{av},j}}{\sum_{j=1}^{N} w_{\mathrm{av},j}}}{\sum_{j=1}^{N} y_j \frac{w_{\mathrm{av},j}}{\sum_{j=1}^{N} w_{\mathrm{av},j}}} \tag{8}$$

Eq. 8 may be recognised as the weighted, discrete analogue of Eq. 5. The choices of M and N were empirical decisions made to keep statistical fluctuations of calculated $\overline{y}_D$ values largely below 2% for a sampling volume diameter of 1000 nm. This limit was not strictly applied to smaller sampling volume diameters, as they produce inherently more variable results and thus the computational cost associated with meeting it was considered unjustified for our purposes.

This process was repeated for the secondary electrons produced by the 250 keV X-rays.

2.6. Neutron RBE

Following Eq. 6, the neutron $\overline{y}_D$ values for each energy and scoring volume were determined by weighting the $\overline{y}_D$ values of each secondary species ($\overline{y}_{D,i}$) by their relative dose contribution d_i. These results were divided by the $\overline{y}_D$ results for the 250 keV X-rays ($\overline{y}_{D,x}$) in the corresponding scoring volume to generate a value for neutron RBE according to Eq. 1:

$$\mathrm{RBE} = \frac{\sum_i d_i \overline{y}_{D,i}}{\overline{y}_{D,x}} \tag{9}$$

Calculated neutron RBE results were compared with published radiation weighting factors for neutrons.

3. Results

3.1. Charged particle spectra

The initial spectra of secondary gammas and charged particles were collected in all three scoring volumes. The spectra of the higher order electrons and positrons stemming from the secondary gammas were also obtained. Fig. 3 shows the secondary particle spectra for the 1 keV, 1 MeV, and 10 MeV neutron sources in all three of the scoring volumes to illustrate trends in the data. Tritons, beryllium ions, and boron ions were excluded from the graphs because their numbers were negligible.

Generally, with increasing depth (Fig. 3 left to right), a lower proportion of protons and heavy ions were liberated relative to gammas.

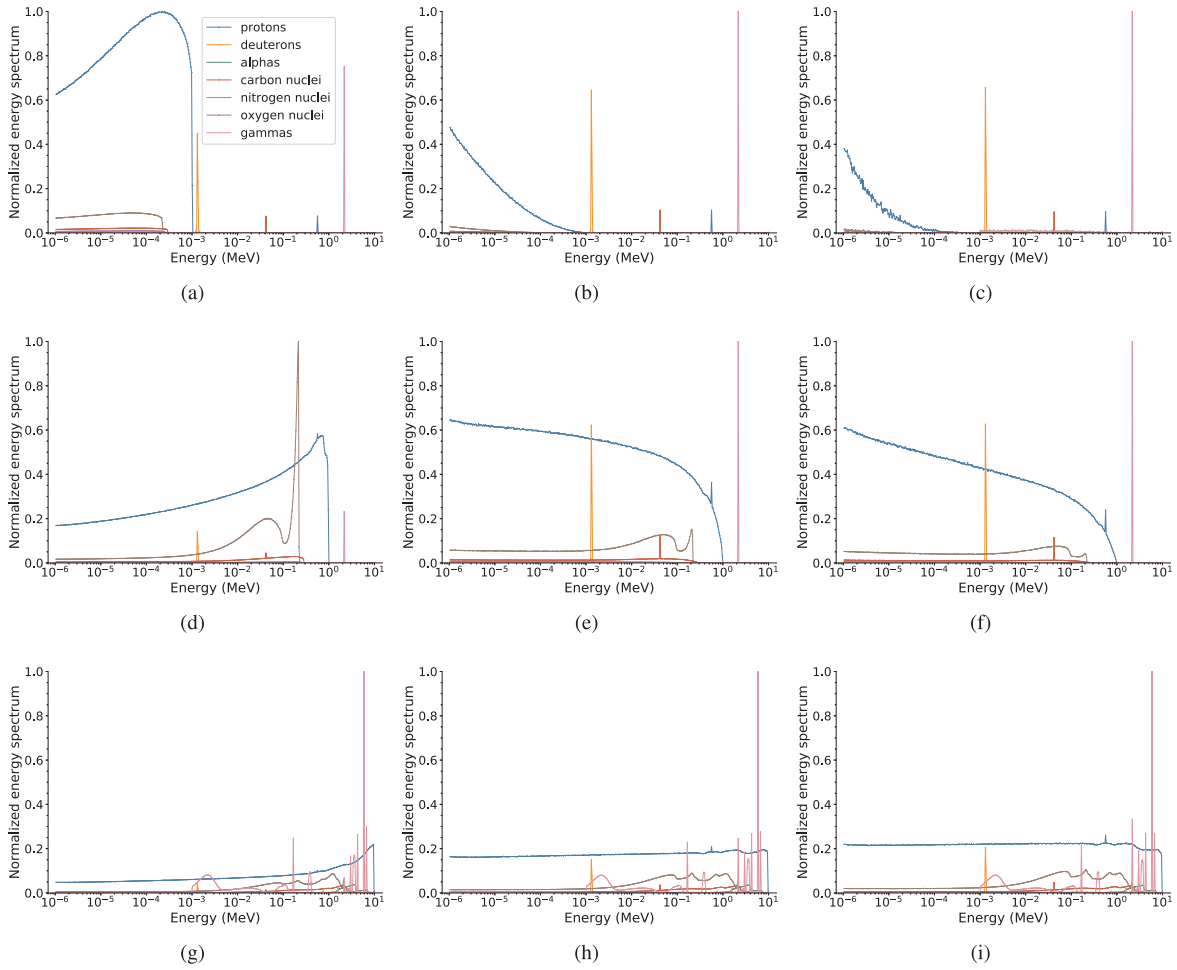

Fig. 3. Secondary charged particle spectra produced in each of the three scoring volumes by three mono-energetic neutron sources. Scoring volumes are shown in increasing depth from left to right; (left) outer, (middle) intermediate, (right) inner. Neutron energies are shown in increasing energy from top to bottom; (top) 1 keV, (middle) 1 MeV, (bottom) 10 MeV. Spectra are normalised to the most probable particle type and energy.

Furthermore, the spectra of these protons and ions was skewed towards lower energies for deeper scoring volumes. A minimal depth dependence across all energies was observed in the shapes of the gamma spectra.

Increasing the incident neutron energy from 1 eV to 2 MeV resulted in higher proportions of protons and heavy ions (Fig. 3 top row to middle row). Further increases of incident neutron energy from 2 MeV to 10 MeV reduced the proportion of protons and yielded larger proportions of gammas and some heavy ions (Fig. 3 bottom row).

The spectra of electrons liberated by secondary gammas during irradiation by 1 keV, 1 MeV, and 10 MeV neutrons in each of the scoring volumes are shown in Fig. 4. Clear peaks occurred at energies of 1 keV and 1 MeV. Neither neutron energy nor phantom depth had much of an effect on the electron spectrum for neutron energies below a few MeV (Fig. 4 top row to middle row). However, as the neutron energy was increased to 10 MeV, the relative height of the 1 MeV peak was reduced (Fig. 4 bottom row). The positron spectra are not shown because their numbers were negligible.

3.2. Relative dose contributions

The relative dose contributions (d_i from Eq. 6) of the secondary species were determined for the neutron energies listed above in each of the three scoring volumes. As can be seen in Fig. 5, most of the dose was deposited by electrons for low energy neutrons. The dominance was especially pronounced in the innermost scoring volume, where the electrons account for approximately all of the dose until about 100 keV (Fig. 5(c)). For all volumes, the proton contribution eventually overtook the electron contribution at high neutron energies, and together the two particles were responsible for a large majority of the dose across the entire range of neutron energies. The deeper the scoring volume, the higher the energy of the proton-electron cross-over point and the larger the predominance of electrons below it. At neutron energies of a few hundred keV and above, the oxygen contribution also became relevant, peaking at about 18% of the total dose in the outer scoring volume for 1 MeV neutrons (Fig. 5(a)). Alphas were only relevant at 5 and 10 MeV, making up between 1% and 6% of the dose in this energy range depending on the scoring volume. Like the rest of the heavy ions, carbons were more prevalent at all energies for scoring volumes closer to the surface. In the outer volume, carbons are responsible for about 1–2% of the dose across the whole energy range (Fig. 5(a)), while they contribute far less below 1 MeV for the other two volumes (Figs. 5(b)-(c)).

Relative dose contributions are not shown for the 250 keV X-rays as all of the energy was deposited by electrons in each of the volumes.

3.3. Dose-mean lineal energies

3.3.1. Neutron secondaries

The $\overline{y}_D$ of the secondary proton, electron, and alpha particle spectra were calculated via the weighted track-sampling algorithm as described in Section 2.5. Tracks were simulated for all proton and electron spectra. Alpha particle tracks were only simulated for the spectra

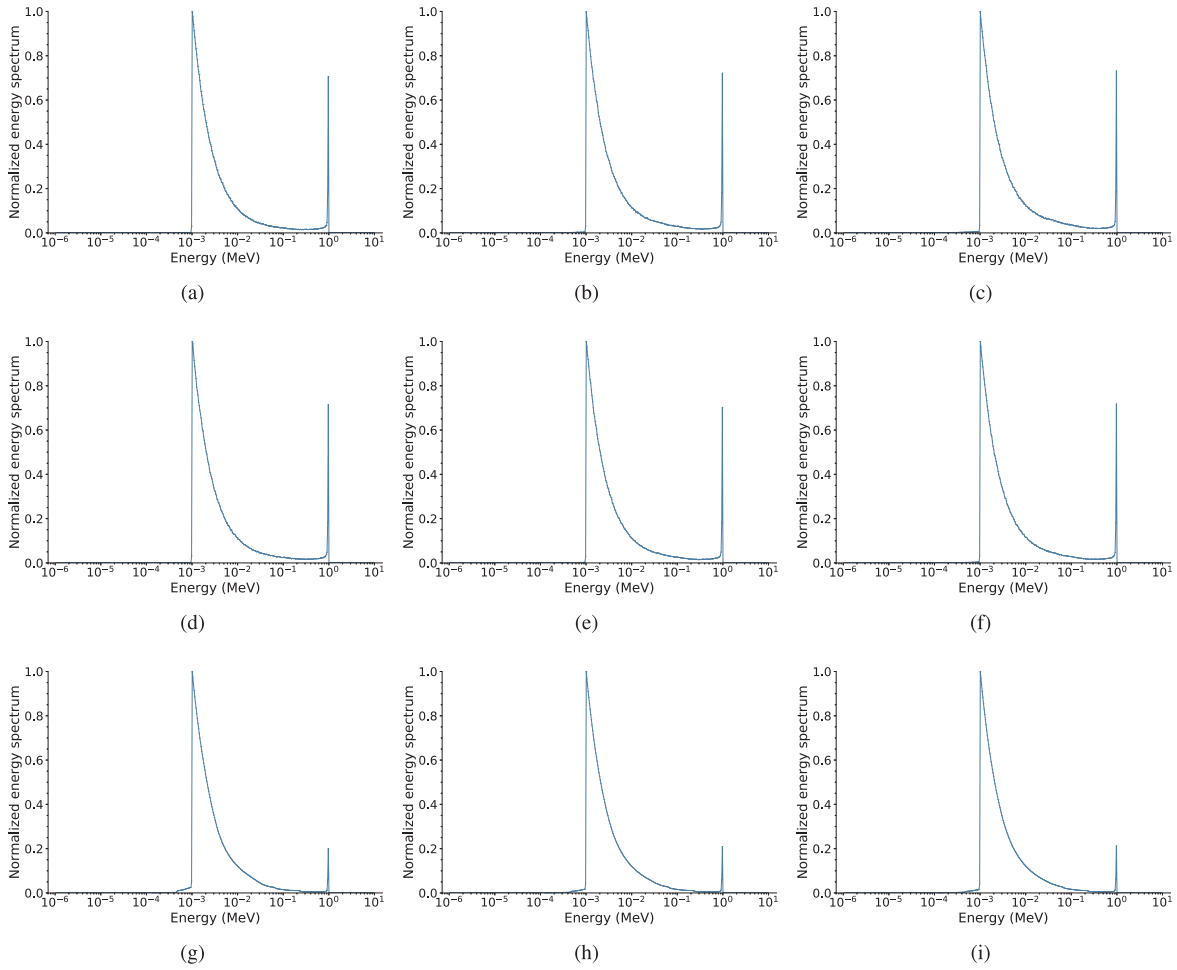

Fig. 4. Spectra of electrons produced by secondary gammas in each of the three scoring volumes after irradiation by mono-energetic neutron sources. Scoring volumes are shown in increasing depth from left to right; (left) outer, (middle) intermediate, (right) inner. Neutron energies are shown in increasing energy from top to bottom; (top) 1 keV, (middle) 1 MeV, (bottom) 10 MeV. Spectra are normalised to the most probable electron energy.

generated by 5 and 10 MeV neutron sources because their contributions to neutron $\overline{y}_D$ were considered negligible at lower neutron energies and thus the increase in computation time was unjustified.

As a representative data set, species-specific $\overline{y}_D$ values obtained using the 1000 nm diameter sampling spheres (largest) are shown in Fig. 6 for all three scoring volumes. In all scoring volumes, the proton $\overline{y}_D$ was larger than the electron $\overline{y}_D$ at all neutron energies tested, while the alpha $\overline{y}_D$ was greater still. The electron $\overline{y}_D$ was approximately constant at all depths from 1 eV to 2 MeV but rose slightly as the neutron energy increased towards 10 MeV. Proton $\overline{y}_D$ was approximately constant in the deeper scoring volumes (Figs. 6(b)-(c)); however, there are a few notable features. As neutron energy increased, the $\overline{y}_D$ of the proton spectra displayed a minimum. With increasing depth, this minimum occurred at higher energies and was less pronounced. Above the minimum energy, the proton $\overline{y}_D$ rose towards a local maximum and a subsequent fall-off. The $\overline{y}_D$ peak, occurring between 0.5 and 0.8 MeV for all volumes, did not extend much higher than the values at low neutron energies (if at all) but was accentuated by a sharp decrease in $\overline{y}_D$ to either side. For the alphas, the $\overline{y}_D$ arising from 5 MeV neutrons was greater than that arising from the 10 MeV neutron-generated spectrum in all volumes.

The variation of proton $\overline{y}_D$ with sampling sphere diameter is shown in Fig. 7. In general, decreasing the sampling diameter resulted in the minimum and peak being less pronounced and occurring at lower energies. For the inner volume, $\overline{y}_D$ increased with increasing sampling diameter for all neutron energies up to 100 nm, although the 30 nm and 100 nm results were nearly identical (Fig. 7(c)). A further increase to 1000 nm resulted in a decrease in $\overline{y}_D$. Similar trends were seen in the shallower volumes; however, there was some cross-over due to the sharp reduction in the depth of the minimum and slope of the post-peak fall-off with decreasing sampling diameter.

Fig. 8 shows the variation of $\overline{y}_D$ with sampling diameter for the electron spectra in each of the scoring volumes. Decreasing the sampling volume increased the magnitude without altering its shape in any significant way. The low energy constancy and slight increase at high energies were present in all data sets, although the rise is much less pronounced for the 2 nm sampling volume. Changes in scoring volume depth had no effect for any of the sampling diameters.

3.3.2. 250 keV X-rays

The $\overline{y}_D$ values for the secondary electron spectra produced by the 250 keV X-rays are shown in Fig. 9 as a function of sampling sphere diameter. As electrons were the only particles produced by the X-rays, the $\overline{y}_D$ of their spectra is equivalent to the $\overline{y}_D$ of the X-rays. Increasing the sampling diameter caused a significant reduction in the calculated $\overline{y}_D$. There was a slight depth dependence, with more interior volumes experiencing marginally higher $\overline{y}_D$ values.

3.4. Neutron RBE

The microdosimetrically-predicted neutron RBE proxy results are shown for each scoring volume in Fig. 10 alongside the ICRP [1] and US

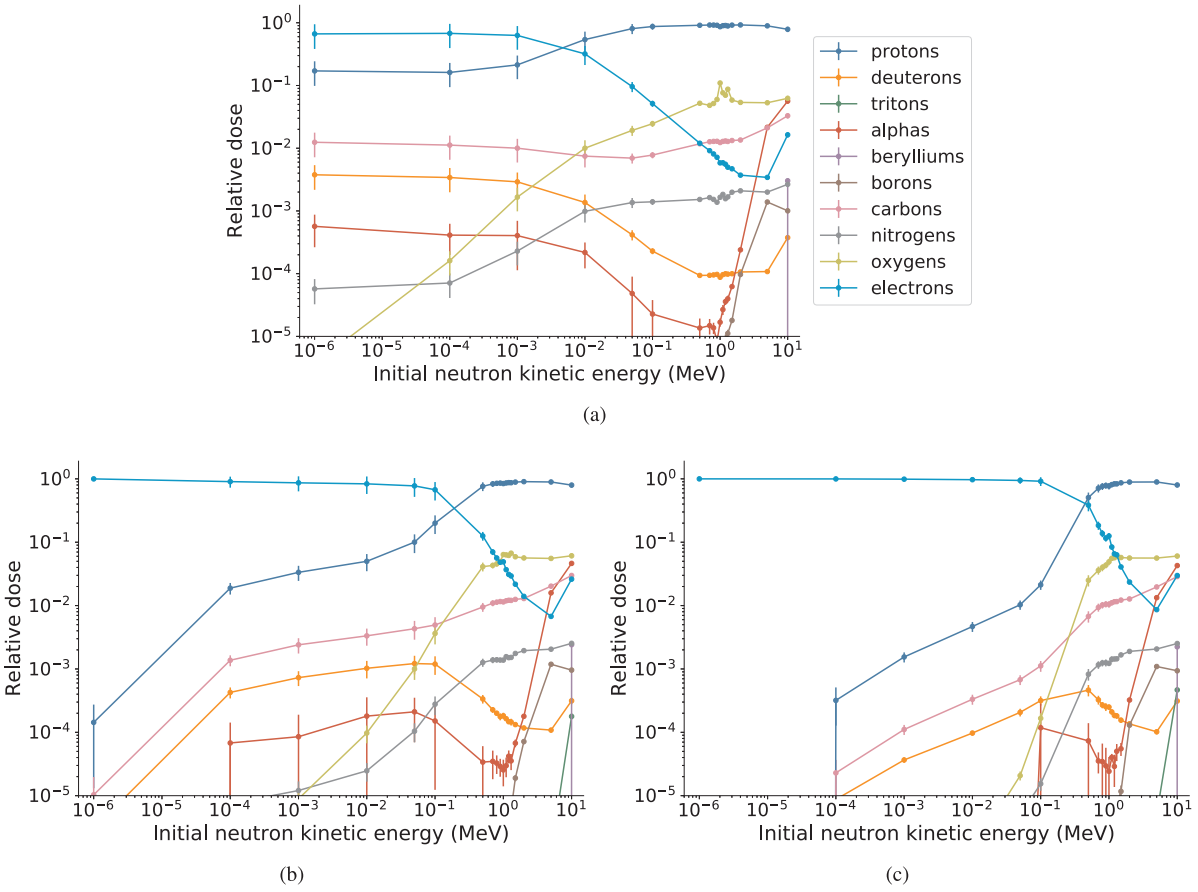

Fig. 5. Relative dose contributions as calculated by the local approximation for each secondary species produced in all three scoring volumes for a range of monoenergetic neutron sources. Error bars are the standard deviation about the mean of 6 runs. Lines are drawn to guide the eye. (a) Outer scoring volume, (b) intermediate scoring volume, (c) inner scoring volume.

NRC [6] radiation weighting factors for neutron energies $E_n \in [1 \times 10^{-6}, 10]$ MeV. For all three scoring volumes, the predicted RBE was relatively low (generally close to 1) and constant in the low energy region (below about 50 keV). A large peak (RBE) then forms, reaching a maximum value near 1 MeV before falling off. With increasing depth, the height of the RBE peak was decreased and shifted to higher energies. All sampling diameters showed roughly the same trend but with varying magnitudes. At low energies, all sampling diameters predict a similar RBE, but the discrepancies became more pronounced at higher neutron energies in the peak region. Here, the smaller the sampling volume the more reduced the peak, with the 2 nm results barely larger than those in the low energy region.

4. Discussion

For incident neutron energies between 1 eV and 10 MeV, two features dominate the shape of the microdosimetrically-predicted RBE proxy graph. First, it can be seen in Fig. 10 that for neutron energies in the intermediate range and below ($\lesssim$ 50 keV), the predicted RBE was low ($\lesssim$ 3) and approximately constant for virtually all sampling diameters in each scoring volume. This trend arose from the predominance of the hydrogen capture reaction (Q = 2.225 MeV) at low energies. Although capture reactions are most probable at thermal energies ($\approx$ 0.025 eV), thermalisation of the neutrons as they traversed the ICRU-4 sphere resulted in a significant number of such interactions for non-thermal initial energies, especially at larger depths. Due to the high energy of the resulting gammas, which can be seen in the peaks near 2.225 MeV in Fig. 3, the dose they deposited exceeded the dose deposited during the thermalisation process. Therefore, the hydrogen capture reaction led to the majority of the neutron dose being deposited by nearly identical electron spectra for low neutron energies (Figs. 4 and 5). As the dose from the X-ray reference radiation was also deposited by electrons and the X-ray $\bar{y}_D$ displayed limited depth dependence, the low-energy neutron fields were microdosimetrically similar to the X-ray fields for all scoring volumes. Furthermore, every increase in neutron-generated electron $\bar{y}_D$ with decreasing sampling diameter (Fig. 8) was balanced by a corresponding increase in the X-ray electron spectra $\bar{y}_D$ (Fig. 9). The net result was that neutron RBE was relatively low and independent of both neutron energy and sampling diameter for all scoring volumes at low energies. The results were in qualitative agreement with the ICRP and US NRC radiation weighting factors, both of which recommend a low, constant RBE at these energies. The agreement is strongest in the outer volume, where elastically scattered protons result in slightly higher predicted RBE values than in the other volumes.

The second trend in the microdosimetrically-predicted neutron RBE proxy graph was the prominent peak centred at energies near 1 MeV (Fig. 10). As the proton dose contribution began to dominate over the electron contribution (Fig. 5), the significantly larger $\bar{y}_D$ of the proton spectra (see Fig. 6 for example) was reflected in an increase in predicted neutron RBE. The peak coincided with the maximum in the proton $\bar{y}_D$ results for each sampling diameter (compare to Fig. 7). For neutrons between 1 eV and 10 MeV, the major sources of protons are (i) elastic scattering with hydrogen nuclei, (ii) the nitrogen capture reaction (Q = 0.626 MeV), and (iii) various inelastic reactions with carbon, nitrogen, and oxygen. As the lowest inelastic threshold for the three heavy nuclei is the 2.311 MeV level of nitrogen, the peak cannot have arisen from inelastic reactions. Furthermore, the low abundance of

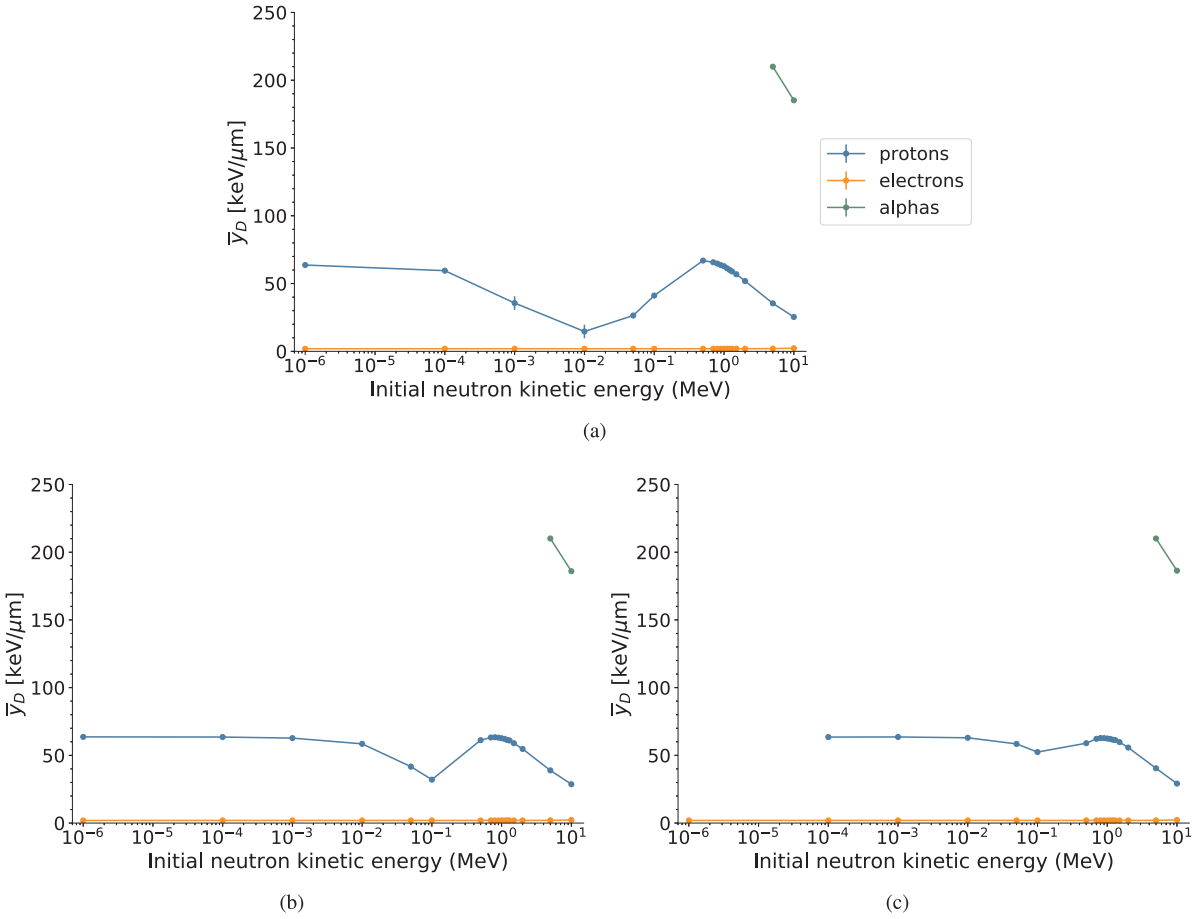

Fig. 6. Calculated $\bar{y}_D$ for the secondary proton, electron, and alpha spectra produced by a range of mono-energetic neutron sources within each scoring volume. Values are given for a spherical sampling diameter of 1000 nm, as an example. Error bars are inter-run standard deviations about the mean of 3 runs. Lines are drawn to guide the eye. (a) Outer scoring volume, (b) intermediate scoring volume, (c) inner scoring volume.

nitrogen capture protons (Q = 0.626 MeV), which can be inferred from both Fig. 3 (negligible proton peak at 0.626 MeV) and from the decrease in proton dose contribution with increasing depth observed in Fig. 5 (see thermalisation discussion), leads to the conclusion that the neutron RBE peak arose from elastically-scattered recoil protons. In contrast to the electrons, the effect of sampling diameter on proton $\bar{y}_D$ was far less pronounced (Fig. 7). Consequently, the relative difference between proton and electron $\bar{y}_D$ increases with increasing sampling diameter. This can be seen in Fig. 10 from the increase in RBE and the steepness of the rise towards it for larger sampling diameters.

Strong qualitative agreement was seen with both the ICRP and the US NRC radiation weighting factors. The ICRP recommend a sharper and more prominent 1 MeV peak than do the US NRC and thus the shape of the ICRP graph was better described by a larger sampling volume. Namely, the ICRP radiation weighting factors most closely resemble the 1000 nm sampling diameter results, while the US NRC radiation weighting factors were best described by the 100 nm sampling diameter results. The fact that the two sets of radiation weighting factors were best described by different sampling diameters highlights an important point about microdosimetry: due to the spatial dependence of the biological consequences of radiation-induced DNA damage, no single sampling volume size can predict all biological effects. However, it should be stressed that the values presented here should be understood only as a means of providing confidence in the trends identified in the constituent data sets (spectra, doses, and $\bar{y}_D$'s), rather than as a quantitative assessment of true neutron RBE. In this regard, the results presented here are in agreement with explanations of the energy dependence of neutron RBE [28], secondary dose contributions [61], and are in line with conventional thinking on neutron dose deposition (see Podgoršak [52]).

Although the major findings of this work provide further support for the neutron RBE model detailed in Baiocco et al. [28], there are some noticeable differences in the data that will be addressed in the following paragraphs. General variations are expected due to the choice of MC toolkit (PHITS vs. Geant4), as this results in the use of different cross sections, physics models, etc. for handling neutron transport. Furthermore, distinct microdosimetric approaches were taken. While Baiocco et al. [28] did employ MCTS to study the neutron-induced secondaries, they did so in the context of DNA damage simulations and not as part of their microdosimetry study. Instead, they utilised the well-established PHITS microdosimetry function [62], which is able to calculate lineal energy (among other microdosimetric parameters) for a large number of particles over broad energy ranges. It does so by extrapolating from a track structure library that combines the results of analytical approximations for the core of an ion track with simulated tracks of the predicted secondary electrons generated using the TRACEL [63] MC code [62]. Data were collected for protons, helium ions, carbon ions, and iron ions with energies between 1 MeV/u and 100 GeV/u [62]. Discrepancies are expected to be minor; however, it is clear that exact agreement is unlikely with the approach taken in this work.

It should also be noted that in their final results, Baiocco et al. [28] report saturation-corrected dose-mean lineal energy y^* [35], an empirical correction to $\bar{y}_D$ that reduces the weight of high lineal energy values (>100–200 keV/μm) in order to account for the so-called overkill effect observed in radiobiology experiments [64]. This is achieved by way of a saturation parameter chosen according to details of the

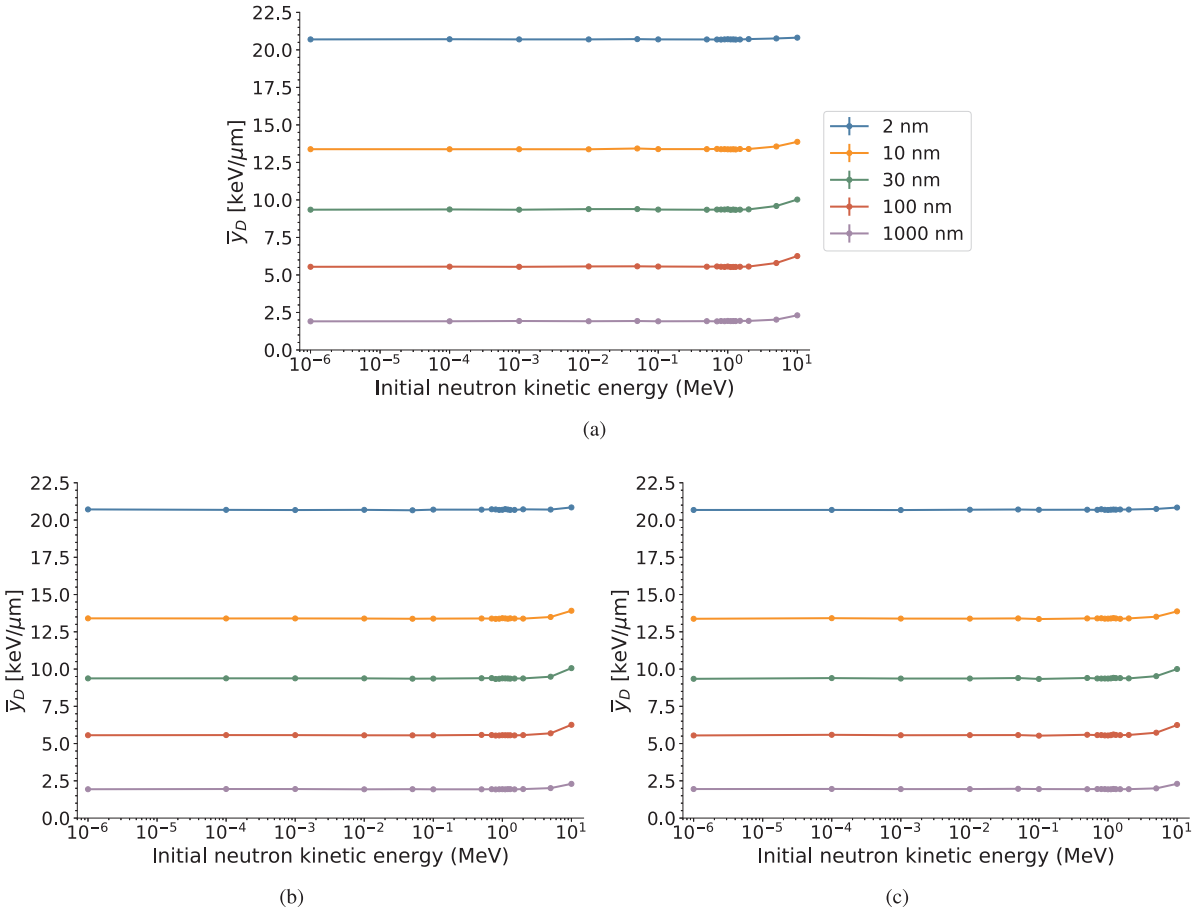

Fig. 7. Calculated $\bar{y}_D$ values of the proton spectra generated in each scoring volume by a range of mono-energetic neutron sources for several spherical sampling volume diameters. Error bars are inter-run standard deviations about the mean of 3 runs. Lines are drawn to guide the eye. (a) Outer scoring volume, (b) intermediate scoring volume, (c) inner scoring volume.

biological system under study [65]. At lower lineal energy values, y^* is roughly equal to $\bar{y}_D$ [64] and thus its use does not provide additional benefit, especially when the choice of saturation parameter is unclear. However, when heavy ions play an important role in the study, as they did in Baiocco et al. [28], y^* is often preferable. In the context of this work, the use of y^* was deemed unnecessary, as high LET particles did not contribute significantly to the results over the majority of the energy range studied.

Compared to Baiocco et al. [28], this work reported a stronger depth dependence of the proton and heavier ion dose contributions at low neutron energies that resulted in significantly lower contributions within the inner scoring volume. This is likely because we generated all of the primary neutrons external to the ICRU sphere, rather than exposing it to the isotropic field specified in Baiocco et al. [28]. While such a difference in irradiation conditions would naturally be associated with a more pronounced depth dependence due to the increased energy moderation, further work is required to fully characterize the effect. It was also found that the proton-electron cross-over point occurred at a notably lower energy than was reported by Baiocco et al. [28] at all three depths. The difference in irradiation conditions likely had an influence on these results, but the fact that the discrepancy extends to the outer scoring volume implies that there are other factors to consider. For example, the method of dose calculation may influence the cross-over point. The local approximation used in this work may have led to inaccuracies, especially in the handling of high-energy electrons. However, the combination of the negligible radiative yield of sub-1 MeV electrons in human tissue (< 1% in ICRU four-component soft tissue [66]) and the requirement that CPE, at least in a practical sense, only exist across the scoring volumes rather than at each point in the ICRU sphere, implies that the use of the local approximation should play only a minor role in the position of the proton-electron cross-over. Finally, it should be noted that at these energies the ratio of electron to proton dose is heavily dependent on the cross sections and sampling methods used by the chosen MC toolkit for the proton capture and scattering reactions with neutrons.

A notable finding in this work was the presence of a local minimum in proton $\bar{y}_D$ (Figs. 6 and 7) between the approximately 1 MeV peak and epithermal energies for nearly all sampling volumes. The fall-off above and below the 1 MeV peak is expected for a spectrum of elastically-scattered protons, while the rise at lower energies appears to provide evidence for an increased importance of nitrogen capture protons. The presence of the minimum, then, is simply the region where elastic scattering gives way to nitrogen capture and the relatively high $\bar{y}_D$ of the protons produced by this reaction. This explanation is consistent with the decrease in magnitude of the minimum as well as its shift towards higher energies with increasing depth, both characteristic of increased moderation. The moderation argument goes some way in explaining the lack of this feature in the Baiocco et al. [28] results as well, although at no point was it completely eliminated for the corresponding 1000 nm sampling volume case in this work. A counter-argument is that Figs. 3(a)–(c) show that the contribution from the nitrogen capture reaction appears to be small, even at low energies. A study of the dose contributions from the different proton interactions in this energy range would be a useful next step in explaining this feature and will be the subject of future work.

The pipeline developed in this work presents a few desirable

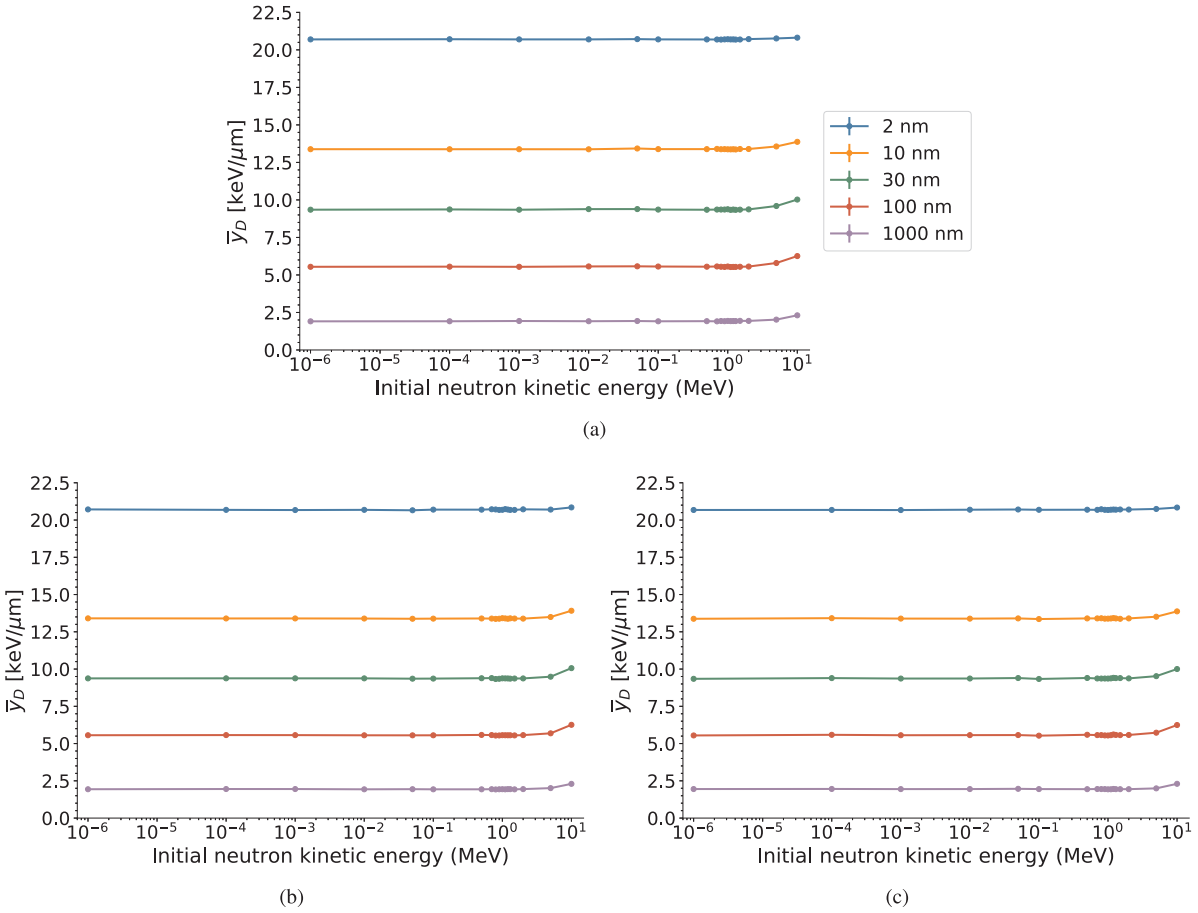

Fig. 8. Calculated $\bar{y}_D$ values of the electron spectra generated in each scoring volume by a range of mono-energetic neutron sources for several spherical sampling volume diameters. Error bars are inter-run standard deviations about the mean of 3 runs. Lines are drawn to guide the eye. (a) Outer scoring volume, (b) intermediate scoring volume, (c) inner scoring volume.

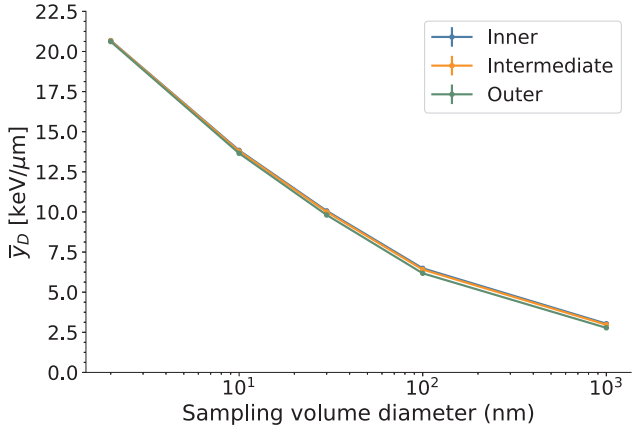

Fig. 9. Calculated $\bar{y}_D$ values as a function of spherical sampling volume diameter for the electron spectra produced by 250 keV X-rays (and thus of the X-rays themselves) in each of the scoring volumes. Error bars are inter-run standard deviations about the mean of 3 runs and are contained within the data points. Lines are drawn to guide the eye.

features as an MCTS tool. On the microdosimetry side, it provides a flexible framework that can be readily adapted to incorporate advances in MCTS cross sections and low-energy transport models. Moreover, the extensibility of Geant4-DNA allows for the implementation of improvements in track sampling techniques, e.g. the associated volume calculation presented here. With respect to the workflow, such an approach allows for multiple MCTS analysis techniques to be readily compared. Our group aims to use these results as a point of reference for our current efforts in DNA damage simulations. However, explicit track generation methods are not without their limitations. For example, the lack of high-energy electron models in Geant4-DNA necessitated a specialised treatment of electron spectra. Treating high-energy electrons as collections of low-energy electrons likely led to a slight, systematic overestimation of electron $\bar{y}_D$, as electron $\bar{y}_D$ generally increases with decreasing energy [34]. Furthermore, the use of Geant4 hard electron–electron collision models in the slowing down process led to a lower energy cut-off of 1 keV for the higher-order electrons (hence the peaks seen in Fig. 4). The effect of this cut-off on the overall electron $\bar{y}_D$ is unclear.

A further limitation on the study of neutrons with Geant4-DNA is the lack of available models for the low-energy transport of heavy ions. In fact, this is an important issue within the MCTS community as a whole and is the subject of ongoing efforts. For example, Liamsuwan and Nikjoo [67] extended the MCTS code KURBUC [58] to include a thorough handling of carbon ion transport into the keV/u range, while the authors of PARTRAC [68] have recently implemented a more general, approximate method for low-energy transport that applies to a wider range of heavy ions [69]. Although the latter approach provides a possible avenue for neutron studies at present [28], previous MCTS results have shown success in ignoring the effects of heavy ions up to incident neutron energies of 14 MeV [70]. Indeed, the results of Section 3.4 strengthen the evidence that, up to several MeV at least, considering only protons, electrons, and alphas is sufficient for the qualitative assessment of certain trends observed in neutron RBE data. However,

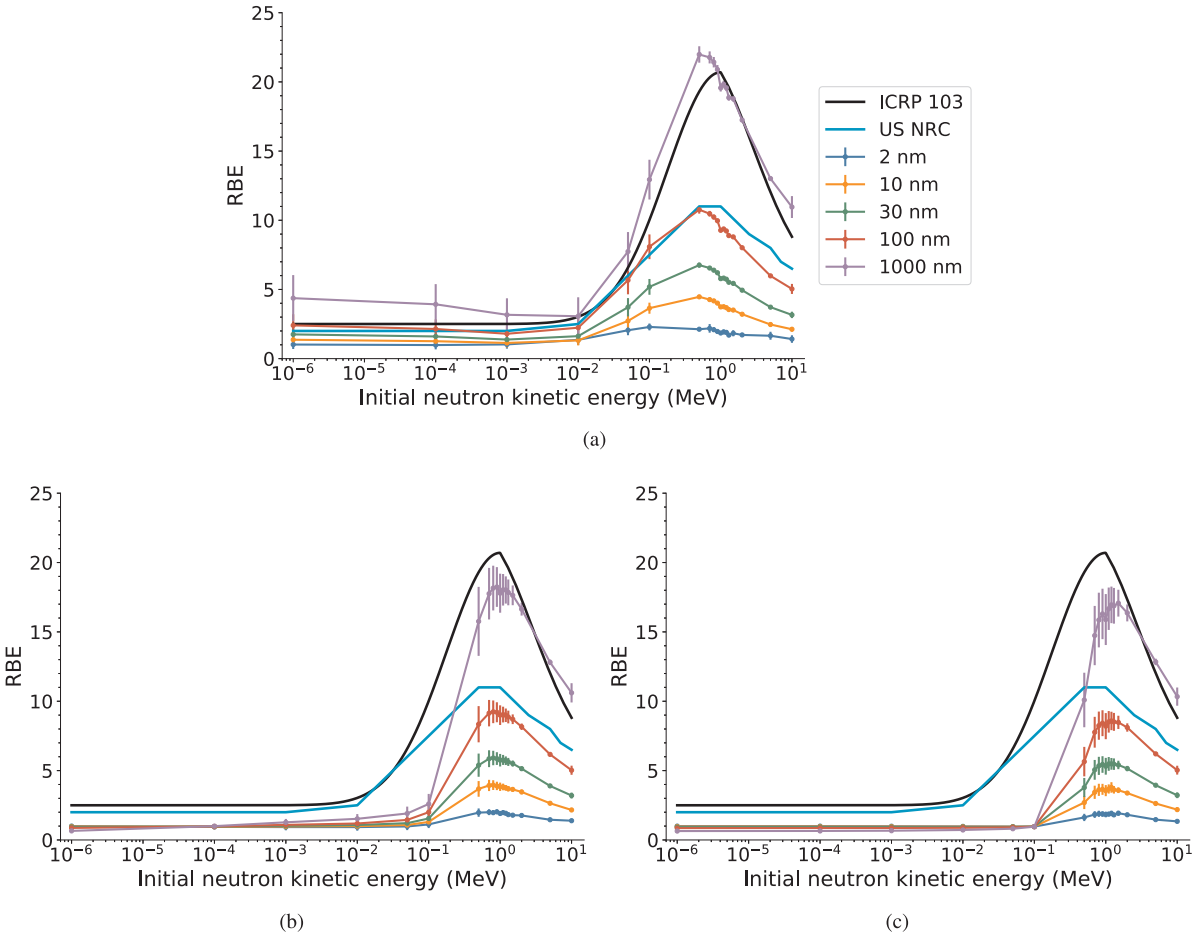

Fig. 10. Predicted neutron RBE, as calculated by Eq. 9, for a range of mono-energetic neutron sources and spherical sampling volume diameters in all three scoring volumes considered. The current ICRP [1] and US NRC [6] radiation weighting factors are plotted for qualitative comparison. Error bars were determined by propagating the inter-run standard deviations of each of the component data sets. Lines are drawn to guide the eye. (a) Outer scoring volume, (b) intermediate scoring volume, (c) inner scoring volume.

caution must be taken in doing so, because the results of Section 3.2 indicate that particles other than protons, electrons, and alpha particles make up well over 1% of the total dose at neutron energies as low as 1 MeV.

5. Conclusions

This work investigated the energy and depth dependence of neutron RBE for carcinogenesis in the context of HERTX by comparing the $\bar{y}_D$ of mono-energetic neutrons incident on a tissue phantom to that of 250 keV X-rays for a number of sampling volume diameters. The results were obtained via a simulation pipeline that combined condensed history simulations with an MCTS code featuring a weighted track-sampling algorithm that operated on charged particle spectra and corrected for biases towards smaller tracks and regions denser in transfer points.

Qualitative agreement was found with the experimentally and epidemiologically derived neutron weighting factors of the ICRP and US NRC for all depths and sampling volume diameters. It was shown that the low, flat portion of the weighting factor graphs below 100 keV resulted from the high cross section and energy transfer of the hydrogen capture reaction, while the peak near 1 MeV was primarily the result of neutron–hydrogen direct elastic scattering. These findings are in agreement with those of Baiocco et al. [28], providing evidence for their *ab initio* explanation of neutron RBE. Decreasing the sampling volume diameter tended to decrease the $\bar{y}_D$ for each particle and had an especially marked effect on the RBE peak. For all sampling volumes, RBE was larger at shallower depths due to a reduced likelihood of thermalisation and thus a higher proportion of secondary ions relative to secondary gammas.

Neutron microdosimetry in Geant4-DNA is currently limited by the energy range of TS models for heavy ions. This issue will require a great deal of attention and effort in the future. However, the ability to examine biological trends by studying only protons, electrons, and alphas shows that Geant4-DNA is already sophisticated enough for many studies. As a standalone tool, the weighted track-sampling algorithm implementation may find uses in other microdosimetric applications. It can be readily adapted for the calculation of other quantities or the recording of full distributions. Improvement efforts should focus on an implementation of the general solution to the calculation of the union of an arbitrary set of spheres described by Cazals et al. [71].

Funding

This work was supported by the CREATE Medical Physics Research Training Network grant of the Natural Sciences and Engineering Research Council of Canada (Grant No.: 432290) and by the National Sciences and Engineering Research Council of Canada Discovery Grant of John Kildea.

Declaration of Competing Interest

The authors declare that they have no known competing financial

interests or personal relationships that could have appeared to influence the work reported in this paper.

Acknowledgements

The authors would like to thank Dr. Piotr Pater and Dr. Shirin Enger for providing insight into numerical microdosimetry and Mr. Felix Mathew, MSc, for helpful discussions regarding implementation details.

References

[1] ICRP, The 2007 Recommendations of the International Commission on Radiological Protection. ICRP Publication 103. Annals of the ICRP 37; 2007.
[2] Kry SF, Bednarz B, Howell RM, Dauer L, Followill D, Klein E, et al. AAPM TG 158: Measurement and calculation of doses outside the treated volume from external-beam radiation therapy. Med Phys 2017;44:e391–429. https://doi.org/10.1002/mp.12462.
[3] Kry SF, Salehpour M, Followill DS, Stovall M, Kuban DA, White RA, Rosen II. Out-of-field photon and neutron dose equivalents from step-and-shoot intensity-modulated radiation therapy. Int J Rad Oncol Biol Phys 2005;62:1204–16.
[4] Montgomery L, Evans M, Liang L, Maglieri R, Kildea J. The effect of the flattening filter on photoneutron production at 10 MV in the Varian TrueBeam linear accelerator. Med Phys 2018;45:4711–9. https://doi.org/10.1002/mp.13148.
[5] Maglieri R, Licea A, Evans M, Seuntjens J, Kildea J. Measuring neutron spectra in radiotherapy using the nested neutron spectrometer. Med Phys 2015;42:6162–9. https://doi.org/10.1118/1.4931963.
[6] US NRC, NRC Regulations Title 10, Code of Federal Regulations: 10 CFR. §20.1004. URL: https://www.nrc.gov/reading-rm/doc-collections/cfr/; 2014.
[7] Incerti S, Douglass M, Penfold S, Guatelli S, Bezak E. Review of Geant4-DNA applications for micro and nanoscale simulations. Physica Medica 2016;32:1187–200. https://doi.org/10.1016/j.ejmp.2016.09.007.
[8] Villegas F, Bäckström G, Tilly N, Ahnesjö A. Energy deposition clustering as a functional radiation quality descriptor for modeling relative biological effectiveness. Med Phys 2016;43:6322–35. https://doi.org/10.1118/1.4966033.
[9] Nikjoo H, Emfietzoglou D, Liamsuwan T, Taleei R, Liljequist D, Uehara S. Radiation track, DNA damage and response a review. Rep Progress Phys 2016;79:116601. https://doi.org/10.1088/0034-4885/79/11/116601.
[10] Friedland W, Schmitt E, Kundrat P, Dingfelder M, Baiocco G, Barbieri S, Ottolenghi A. Comprehensive track-structure based evaluation of DNA damage by light ions from radiotherapy-relevant energies down to stopping. Sci Rep 2017;7:1–15. https://doi.org/10.1038/srep45161.
[11] Meylan S, Incerti S, Karamitros M, Tang N, Bueno M, Clairand I, Villagrasa C. Simulation of early DNA damage after the irradiation of a fibroblast cell nucleus using Geant4-DNA. Sci Rep 2017;7. https://doi.org/10.1038/s41598-017-11851-4.
[12] Lampe N, Karamitros M, Breton V, Brown JMC, Sakata D, Sarramia D, Incerti S. Mechanistic DNA damage simulations in Geant4-DNA part 2: electron and proton damage in a bacterial cell. Physica Medica 2018;48:146–55. https://doi.org/10.1016/j.ejmp.2017.12.008.
[13] Schuemann J, McNamara A, Warmenhoven J, Henthorn N, Kirkby KJ, Merchant MJ, et al. A new standard DNA damage (SDD) data format. Rad Res 2019;191:76–92. https://doi.org/10.1667/rr15209.1.
[14] Pihet P, Menzel HG, Schmidt R, Beauduin M, Wambersie A. Biological weighting function for RBE specification of neutron therapy beams. Intercomparison of 9 European centres. Rad. Protection Dosimetry 1990;31:437–42. https://doi.org/10.1093/oxfordjournals.rpd.a080709.
[15] Menzel HG, Wambersie A, Pihet P. The clinical RBE and microdosimetric characterization of radiation quality in fast neutron therapy. Acta Oncologica 1994;33:251–9. https://doi.org/10.3109/02841869409098415.
[16] Pignol JP, Slabbert J, Binns P. Monte Carlo simulation of fast neutron spectra: Mean lineal energy estimation with an effectiveness function and correlation to RBE. Int J Rad Oncol Biol Phys 2001;49:251–60. https://doi.org/10.1016/S0360-3016(00)01406-1.
[17] Paganetti H, Olko P, Kobus H, Becker R, Schmitz T, Waligorski MP, Filges D, Müller-Gärtner HW. Calculation of relative biological effectiveness for proton beams using biological weighting functions. Int J Rad Oncol Biol Phys 1997;37:719–29. https://doi.org/10.1016/S0360-3016(96)00540-8.
[18] Gerlach R, Roos H, Kellerer AM. Heavy ion RBE and microdosimetric spectra. Rad. Protection Dosimetry 2002;99:413–8. https://doi.org/10.1093/oxfordjournals.rpd.a006821.
[19] Zaider M, Brenner DJ. On the microdosimetric definition of quality factors. Rad Res 1985;103:302–16. https://doi.org/10.2307/3576753.
[20] Lindborg L, Grindborg JE. Nanodosimetric results and radiotherapy beams: a clinical application? Rad Protection Dosimetry 1997;70:541–6. https://doi.org/10.1093/oxfordjournals.rpd.a032013.
[21] Lindborg L, Nikjoo H. Microdosimetry and radiation quality determinations in radiation protection and radiation therapy. Rad Protection Dosimetry 2011;143:402–8. https://doi.org/10.1093/rpd/ncq390.
[22] Zaider M, Varma MN. Carcinogenic risk coefficients at environmental levels of radon exposures: a microdosimetric approach. Health Phys 1996;70:837–44. https://doi.org/10.1097/00004032-199606000-00009.
[23] Lindborg L, Hultqvist M, Carlsson Tedgren Å, Nikjoo H. Lineal energy and radiation quality in radiation therapy: model calculations and comparison with experiment. Phys Med Biol 2013;58:3089–105. https://doi.org/10.1088/0031-9155/58/10/3089.
[24] Kellerer AM, Rossi HH. The theory of dual radiation action. Current Topics Rad Res Q arterly VIII 1974:85–158.
[25] Rossi HH, Zaider M. Compound dual radiation action: I. General aspects. Rad Res 1992;132:178–83. https://doi.org/10.2307/3578524.
[26] Wuu CS, Kliauga P, Amols HI. Microdosimetric evaluation of relative biological effectiveness for 103-Pd, 125-I, 241-Am, and 192-Ir brachytherapy sources. International Journal of Radiation Oncology* Biology*. Physics 1996;36:689–97. https://doi.org/10.1016/S0360-3016(96)00374-4.
[27] Wambersie A, Menzel H, Gahbauer R, Jones DTL, Michael BD, Paretzke H. Biological weighting of absorbed dose in radiation therapy. Rad Protection Dosimetry 2002;99:445–52. https://doi.org/10.1093/oxfordjournals.rpd.a006829.
[28] Baiocco G, Barbieri S, Babini G, Morini J, Alloni D, Friedland W, et al. The origin of neutron biological effectiveness as a function of energy. Sci Rep 2016;6. https://doi.org/10.1038/srep34033.
[29] Ottolenghi A, Smyth V, Trott KR. Assessment of cancer risk from neutron exposure–The ANDANTE project. Rad Measure 2013;57:68–73. https://doi.org/10.1016/j.radmeas.2012.10.017.
[30] Sato T, Niita K, Matsuda N, Hashimoto S, Iwamoto Y, Noda S, et al. Particle and heavy ion transport code system, PHITS, version 2.52. J Nucl Sci Technol 2013;50:913–23. https://doi.org/10.1080/00223131.2013.814553.
[31] Agostinelli S, Allison J, Amako K, Apostolakis J, Araujo H, Arce P, Asai M, Axen D, Banerjee S, Barrand G, et al. Geant4a simulation toolkit. Nucl Instrum Methods Phys Res Sect A 2003;506:250–303. URL:https://doi.org/10.1016/S0168-9002(03)01368-8.
[32] Allison J, Amako K, Apostolakis J, Araujo H, Arce Dubois P, Asai M, et al. Geant4 developments and applications. IEEE Trans Nucl Sci 2006;53:270–8. https://doi.org/10.1109/TNS.2006.869826.
[33] Allison J, Amako K, Apostolakis J, Arce P, Asai M, Aso T, et al. Recent developments in GEANT4. Nuclear Instruments and Methods in. Phys Res Sect A 2016;835:186–225. https://doi.org/10.1016/j.nima.2016.06.125.
[34] Famulari G, Pater P, Enger SA. Microdosimetry calculations for monoenergetic electrons using Geant4-DNA combined with a weighted track sampling algorithm. Phys Med Biol 2017;62. https://doi.org/10.1088/1361-6560/aa71f6.
[35] ICRU. Microdosimetry. Tech Rep 1983;36. ICRU.
[36] Nikjoo H, Lindborg L. RBE of low energy electrons and photons. Phys Med Biol 2010;55:R65–109. https://doi.org/10.1088/0031-9155/55/10/R01.
[37] Kellerer AM. Fundamentals of Microdosimetry. Kase K, Bjärngard B, Attix F, editors. The Dosimetry of Ionizing Radiation, vol. 1. Academic Press London; 1985. p. 77–162. https://doi.org/10.1016/B978-0-12-400401-6.X5001-3 chapter 2.
[38] Lindborg L, Waker A. Microdosimetry: experimental methods and applications. Boca Raton, Fl: CRC Press, Taylor and Francis Group; 2017.
[39] Kellerer AM, Chmelevsky D. Concepts of microdosimetry. II. Probability distributions of the microdosimetric variables. Rad Environ Biophys 1975;12:205–16. https://doi.org/10.1007/BF01327348.
[40] Rossi HH, Zaider M. Microdosimetry and its applications. Berlin: Springer-Verlag; 1996.
[41] Chmelevsky D, Kellerer AM. Computation of microdosimetric distributions for small sites. Rad Environ Biophys 1977;14:123–36.
[42] Kyriakou I, Ivanchenko V, Sakata D, Bordage MC, Guatelli S, Incerti S, Emfietzoglou D. Influence of track structure and condensed history physics models of Geant4 to nanoscale electron transport in liquid water. Physica Medica 2019;58:149–54. https://doi.org/10.1016/j.ejmp.2019.01.001.
[43] Bernal MA, Bordage MC, Brown JMC, Davidková M, Delage E, El Bitar Z, et al. Track structure modeling in liquid water: a review of the Geant4-DNA very low energy extension of the Geant4 Monte Carlo simulation toolkit. Physica Medica 2015;31:861–74. https://doi.org/10.1016/j.ejmp.2015.10.087.
[44] Incerti S, Karamitros M, Mantero A, Moretto P, Tran HN, Mascialino B, et al. Comparison of GEANT4 very low energy cross section models with experimetnal data in water. Med Phys 2010;37:4692–708. https://doi.org/10.1118/1.3476457.
[45] Incerti S, Kyriakou I, Bernal MA, Bordage MC, Francis Z, Guatelli S, et al. Geant4-DNA example applications for track structure simulations in liquid water: A report from the Geant4-DNA Project. Med Phys 2018;45. https://doi.org/10.1002/mp.13048.
[46] Incerti S, Baldacchino G, Bernal M, Champion R, Francis C, Guèye Z. The Geant4-DNA project. Int J Model, Simul Sci Comput 2010;1:157–78. https://doi.org/10.1142/S1793962310000122.
[47] ICRU. Tissue substitutes in radiation dosimetry and measurement. Tech Rep 1989;44. ICRU.
[48] Cullen DE, Hubbell JH, Kissel L, EPDL97: the evaluated photo data library 97 version. Technical Report. Lawrence Livermore National Lab., CA. URL: http://reddog1.llnl.gov/homepage.red/photon.htm; 1997.
[49] Perkins ST, Cullen DE, Seltzer SM, Tables and graphs of electron-interaction cross-sections from 10 eV to 100 GeV derived from the LLNL evaluated electron data library (EEDL), Z= 1–100. UCRL-50400 31; 1991a, 21–24.
[50] Perkins ST, Cullen DE, Chen MH, Rathkopf J, Scofield J, Hubbell JH, Tables and graphs of atomic subshell and relaxation data derived from the LLNL Evaluated Atomic Data Library (EADL), Z= 1–100. Technical Report. Lawrence Livermore National Lab., CA; 1991b.
[51] Chadwick MB, Herman M, Obložinský P, Dunn ME, Danon Y, Kahler AC, et al. ENDF/B-VII.1 Nuclear data for science and technology: cross sections, covariances, fission product yields and decay data. Nucl Data Sheets 2011;112. https://doi.org/10.1016/j.nds.2011.11.002.
[52] Podgoršak EB. Radiation physics for medical physicists. 3rd ed. Switzerland: Springer International Publishing; 2016.

[53] ICRP, Conversion Coefficients for use in Radiological Protection against External Radiation. ICRP Publication 74. Annals of the ICRP 26; 1996.
[54] Andreo P, Burns DT, Nahum AE, Seuntjens J, Attix FH, Fundamentals of Ionizing Radiation Dosimetry; 2017.
[55] Emfietzoglou D. Inelastic cross-sections for electron transport in liquid water: a comparison of dielectric models. Rad. Phys. Chem. 2003;66:373–85. https://doi.org/10.1016/S0969-806X(02)00504-2.
[56] Kyriakou I, Incerti S, Francis Z. Improvements in Geant4 energy-loss model and the effect on low-energy electron transport in liquid water. Med Phys 2015;42:3870–6. https://doi.org/10.1118/1.4921613.
[57] Champion C, Incerti S, Aouchiche H, Oubaziz D. A free-parameter theoretical model for describing the electron elastic scattering in water in the Geant4 toolkit. Rad. Phys Chem 2009;78:745–50. https://doi.org/10.1016/j.radphyschem.2009.03.079.
[58] Uehara S, Nikjoo H, Goodhead DT. Cross-sections for water vapour for the Monte Carlo electron track structure code from 10 eV to the MeV region. Phys Med Biol 1993;38:1841. https://doi.org/10.1088/0031-9155/38/12/010.
[59] Michaud M, Wen A, Sanche L. Cross sections for low-energy (1–100 eV) electron elastic and inelastic scattering in amorphous ice. Rad Res 2003;159:3–22. https://doi.org/10.1667/0033-7587(2003)159[0003:CSFLEE]2.0.CO;2.
[60] Melton CE. Cross sections and interpretation of dissociative attachment reactions producing OH-, O-, and H- in H2O. J Chem Phys 1972;57:4218–25. https://doi.org/10.1063/1.1678051.
[61] Satoh D, Takahashi F, Endo A, Ohmachi Y, Miyahara N. Calculation of dose contributions of electron and charged heavy particles inside phantoms irradiated by monoenergetic neutron. J Rad Res 2008;49. https://doi.org/10.1269/jrr.08009.
[62] Sato T, Watanabe R, Sihver L, Niita K. Applications of the microdosimetric function implemented in the macroscopic particle transport simulation code PHITS. Int J Rad Biol 2012;88:143–50. https://doi.org/10.3109/09553002.2011.611216.
[63] Tomita H, Kai M, Kusama T, Ito A. Monte carlo simulation of physicochemical processes of liquid water radiolysis. Rad Environ Biophys 1997;36:105–16. https://doi.org/10.1007/s004110050061.
[64] Kase Y, Kanai T, Matsumoto Y, Furusawa Y, Okamoto H, Asaba T, Sakama M, Shinoda H. Microdosimetric measurements and estimation of human cell survival for heavy-ion beams. Rad Res 2006;166:629–38. https://doi.org/10.1667/RR0536.1.
[65] Baiocco G, Babini G, Barbieri S, Morini J, Friedland W, Villagrasa C, Rabus H, Ottolenghi A. What roles for track-structure and microdosimetry in the era of -omics and systems biology? Rad Protection Dosimetry 2018;183:22–5. https://doi.org/10.1093/rpd/ncy221.
[66] Berger M, Coursey J, Zucker M, Chang J, Stopping-power & range tables for electrons, protons, and helium ions. NIST Standard Reference Database 124, [Online]. Available: https://dx.doi.org/10.18434/T4NC7P [2020, March 4]. National Institute of Standards and Technology; 2017.
[67] Liamsuwan T, Nikjoo H. A monte carlo track structure simulation code for the full-slowing-down carbon projectiles of energies 1 keV u–1–10 MeV u–1in water. Phys Med Biol 2013;58:673–701. https://doi.org/10.1088/0031-9155/58/3/673.
[68] Friedland W, Dingfelder M, Kundrát P, Jacob P. Track structures, DNA targets and radiation effects in the biophysical Monte Carlo simulation code PARTRAC. Mutation Res/Fundam Mol Mech Mutagenesis 2011;711:28–40. https://doi.org/10.1016/j.mrfmmm.2011.01.003.
[69] Schmitt E, Friedland W, Kundrát P, Dingfelder M, Ottolenghi A. Cross-section scaling for track structure simulations of low-energy ions in liquid water. Rad Protection Dosimetry 2015;166:15–8. https://doi.org/10.1093/rpd/ncv302.
[70] Zabihi A, Incerti S, Francis Z, Forozani G, Semsarha F, Moslehi A, et al. Computational approach to determine fast neutrons RBE using the GEANT4-DNA toolkit and a DNA atomic model from the Protein. Data Bank. Physical Review E 2019;99:052404https://doi.org/10.1103/PhysRevE.99.052404.
[71] Cazals F, Harshad K, Loriot S, Computing the Volume of a Union of Balls: a Certified Algorithm. Technical Report RR-7013. INRIA; 2009.